

The 3-D topological signatures and a new discrimination method for single-electron events and $0\nu\beta\beta$ events in CZT: A Monte Carlo simulation study

Ming Zeng^{a,b}, Tenglin Li^{a,b}, Jirong Cang^{a,b}, Zhi Zeng^{a,b,*},
Jianqiang Fu^{a,b}, Jianping Cheng^{a,b}, Hao Ma^{a,b}, Yinong Liu^{a,b}

^a Key Laboratory of Particle & Radiation Imaging(Tsinghua University), Ministry of Education, China

^b Department of Engineering Physics, Tsinghua University, Beijing 100084, China

Abstract

In neutrinoless double beta ($0\nu\beta\beta$) decay experiments, topological signature provides an important method to distinguish double beta events and achieve lower background rates. This article establishes a Monte Carlo (MC) simulation platform to study the topological signatures of single-electron events and $0\nu\beta\beta$ events in CdZnTe. Based on the MC data, a new topological signature of the primary trajectory is proposed and the energy deposition along the trajectory is discussed. Applying new energy deposition models, this article presents a new discrimination method between single-electron and $0\nu\beta\beta$ events, which provides a good background rejection factor as well as a high signal efficiency.

Keywords: $0\nu\beta\beta$, Topological signature, Primary trajectory, CdZnTe

1 Introduction

Research of neutrinoless double beta ($0\nu\beta\beta$) decay is a key approach to answer whether neutrinos are Majorana particles and whether total lepton number is conserved in nature, as well as to provide the direct information about the absolute neutrino mass scale [1]. Several experiments using different $0\nu\beta\beta$ isotopes are already running or about to run, to explore the best strategy for $0\nu\beta\beta$ searches, such as the ^{76}Ge -based GERDA experiment [2], the ^{136}Xe -based EXO-200 experiment [3], the ^{130}Te -based CUORE experiment [4], and so on. The formidable challenges of the experimental approaches are their scalability to large masses, and their capability to control the backgrounds to the required extremely low levels [1].

The COBRA experiment [5] is planning to use a large amount of CdZnTe (CZT) room temperature semiconductor detectors for the search of $0\nu\beta\beta$. CZT contains 9 candidate isotopes for $0\nu\beta\beta$, and among them ^{116}Cd has the highest Q -value of 2813.50 keV. This isotope is the main target of the search, since its Q -value lies above the highest relevant naturally occurring gamma line (^{208}Tl at 2614.6 keV), and thus contributes to the background reduction in the region of interest. Other possible means to reach the extremely low background level [6] could be pixelised detectors, by exploiting the topological information of the events. In Ref [7], the COBRA collaboration developed

* Corresponding author, E-mail: zengzhi@tsinghua.edu.cn

a set of selection criteria between single-electron and $0\nu\beta\beta$ events in pixelated CZT detectors, based on three distributions of the 2-D topological signatures: the number of active pixels, the maximum separation of active pixels, and the variation in the energy deposition. Whereas, these distributions are proposed based on the features of 2-D unorganised pixels, and the 3-D topological signatures of single-electron events and $0\nu\beta\beta$ events in CZT have not been discussed yet.

The NEXT experiment [8] is planning to search $0\nu\beta\beta$ in high pressure xenon gas TPC. One main advantage of this technique is the ability to reconstruct the trajectory of the two electrons emitted in the decays, which contributes to the suppression of backgrounds. In Ref. [9], the NEXT collaboration developed an inspiring algorithm to group the voxels into tracks and find their end-points, and proposed a method to distinguish single electrons and electron-positron pairs based on the energy deposited at the end-points of the track (called a ‘blob’). Whereas, the topological signature of the ‘lower energy blob candidate’ has not taken full advantage of the entire track, and lacks the robustness as a discrimination method.

This article establishes a Monte Carlo simulation platform to simulate the behaviour of the single-electron and $0\nu\beta\beta$ events in CdZnTe, and generates a large quantity of tracks of both event types. Applying the knowledge of graph theory, the *primary trajectory* of a Monte Carlo track is reconstructed from the unorganised points, and is proved to be a crucial topological signature. Based on the energy deposition along the whole length of the *primary trajectory*, two models of the single-electron and $0\nu\beta\beta$ events are built and demonstrated to be well distinguished from each other. As a result, a new discrimination method is proposed, which provides a good background rejection factor as well as a high signal efficiency. The last part of this article discusses the discrimination efficiency affected by the parameters chosen in the algorithm, and confirms the feasibility of the method.

2 The Monte Carlo simulation method

2.1 The methods and basic setup for simulation

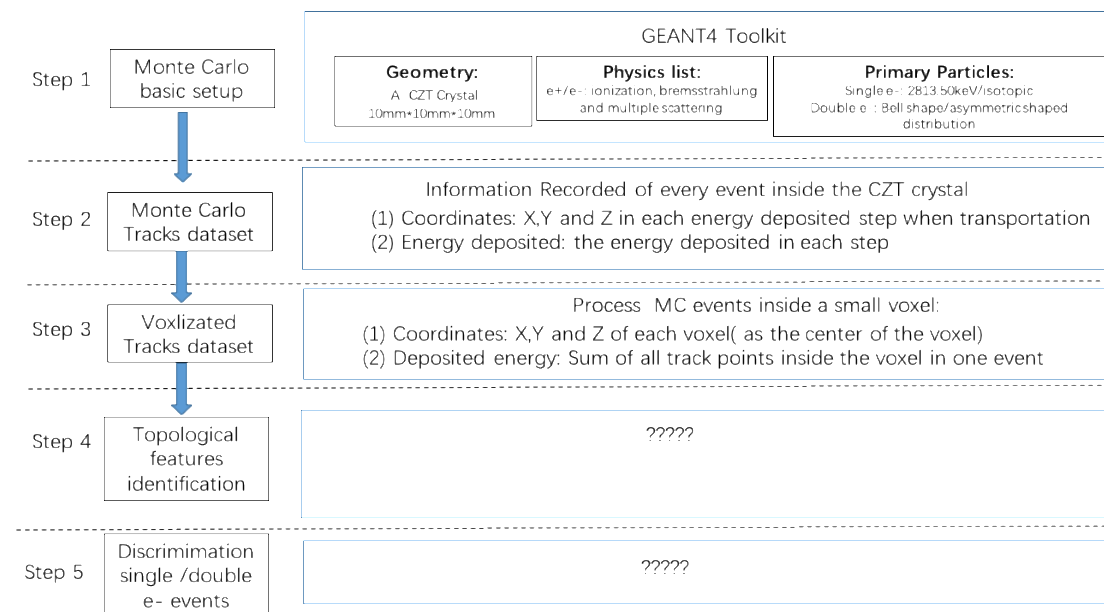


Fig. 0 The whole process of the method and key points in each step

In order to simulate of the behaviour of single-electron events and $0\nu\beta\beta$ events in CZT, the GEANT4 simulation package [10] is used in this article. The Standard physics list is adopted, and the corresponding physical processes affecting electrons are ionization, bremsstrahlung and scattering processes [11].

The size of CZT is $10\text{ mm} \times 10\text{ mm} \times 10\text{ mm}$, which is large enough for most electrons of interested energy to deposit all their energy within the boundaries. Also, a pre-selection is made to exclude the events which don't deposit all the energy in CZT due to bremsstrahlung interactions or other circumstances.

For a single-electron event, the electron is emitted from the center point of CZT, and in a random direction. The initial energy of the electron is 2813.50 keV , corresponding to the Q -value of ^{116}Cd .

For a $0\nu\beta\beta$ event, two electrons are emitted from the central point of CZT simultaneously, with a total energy of 2813.50 keV . As the mechanism of $0\nu\beta\beta$ decay is not well understood yet, there are many hypotheses providing different energy and angular distributions of the two electrons, which were discussed in Ref. [12]. This article considered the *mass mechanism* as the domain mechanism, to stay the same with the choice in Ref. [7]. In this $0\nu\beta\beta$ hypothesis, the energy distribution of each electron is bell shaped and centred on half the Q -value. The angular distribution between the two electrons is asymmetric shaped, and peaks at the opening angle of $\theta = 120^\circ$. The curves of both distributions can be found in Ref [7].

2.2 Monte Carlo Tracks

For every sample of the two event types simulated by GEANT4, the x , y , z -coordinate and energy deposited in every step are recorded. This sample is called a 'Monte Carlo (MC) track' of the single-electron events or $0\nu\beta\beta$ events. An instance of the MC tracks is shown in Fig. 1.

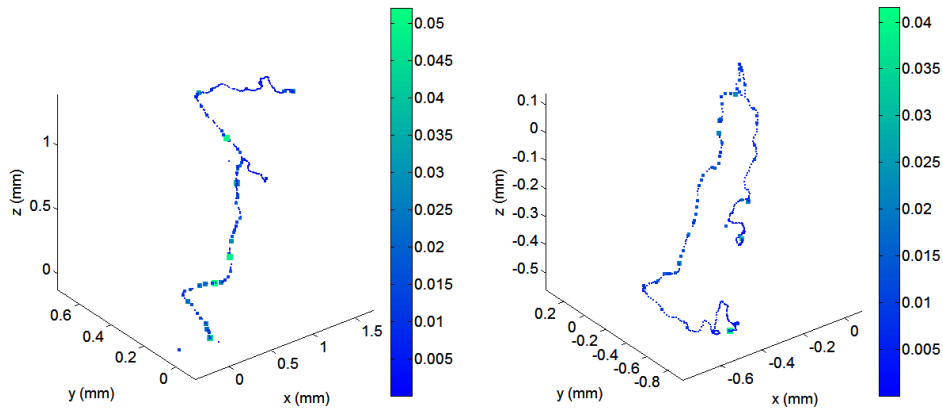


Fig. 1. An instance of the MC tracks of a single-electron event (left) and a $0\nu\beta\beta$ event (right). The size and color of the markers indicate the value of the energy deposition (similarly hereinafter).

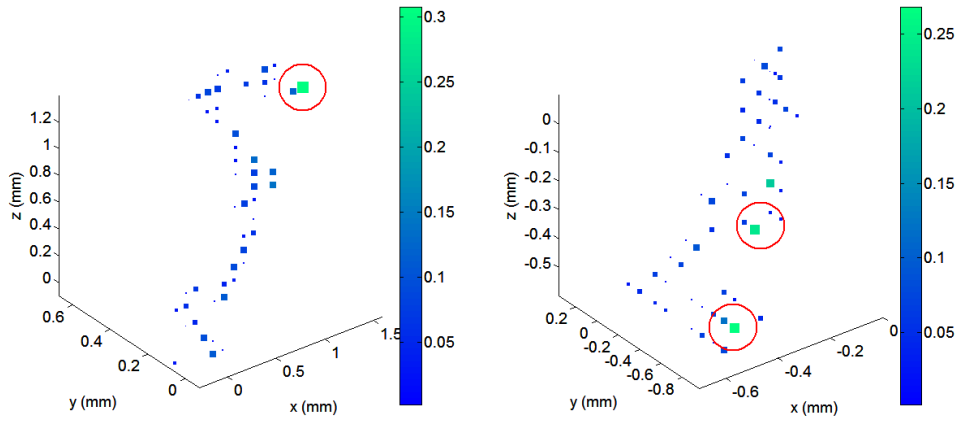


Fig. 2. An instance of the voxelized tracks of a single-electron event (left) and a $0\nu\beta\beta$ event. Energy depositions at the endpoints are characterized by: One larger energy deposition (one blob) at one endpoint of a single-electron event, and two larger energy depositions (two blobs) at both endpoints of a $0\nu\beta\beta$ event.

2.3 Voxelization

To study the topological signatures of the single-electron and $0\nu\beta\beta$ events, the MC tracks are not the proper research subjects. The reason is that the current spatial resolution of a real CZT detector is nowhere close to that of the MC track simulated in GEANT4. Consequently, the topological signature of the MC track may meet big differences from that of the track measured in a real detector.

So the voxelization of the track is conducted, to make a better approximation to a real experiment. The initial voxels are cubes of 0.1 mm in volume ($D = 0.1$ mm, D is the side length of the voxel), corresponding to the best spatial resolution of the CZT-Timepix detector described in Ref. [13].

The concept of voxelization is to replace the MC track by the voxelized track: The coordinate of each point in the voxelized track is given by the central coordinate of the voxel, and the energy of each point is given by the sum of the energy deposited within the voxel's boundaries. An instance of the voxelized tracks is shown in Fig. 2, which are the voxelization of the MC tracks in Fig. 1.

2.4 Spatial end energy distribution of the voxelized track

With the voxelized track, we can estimate some simple 3-D topological signatures: the number of active voxels, the variation in the energy deposition of every voxel, and the maximum separation of active voxels, where an 'active' voxel means a voxel with a non-zero energy deposition. The distributions of these simple topological signatures is shown in Fig. 3, and can be compared with the similar results achieved by the COBRA collaboration for simple 2-D topological signatures in CZT in Ref. [7].

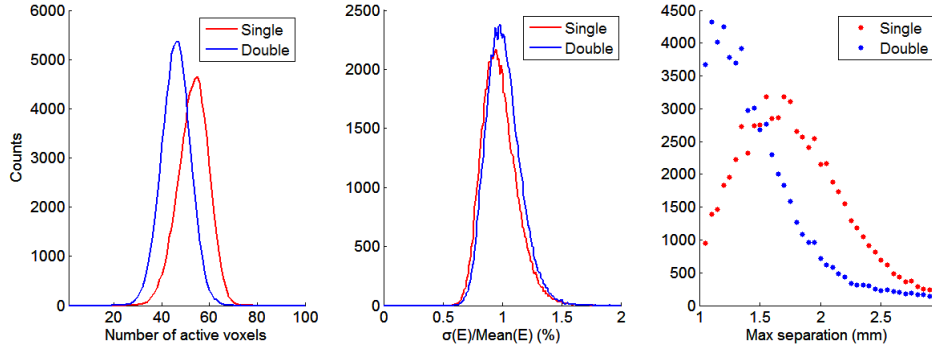


Fig. 3. Distributions of the single-electron events and $0\nu\beta\beta$ events for a voxel size of 0.1 mm and an energy of 2813.50 keV. (Left) The number of voxels which were traversed. (Centre) The standard deviation of the energy divided by the mean energy (in percent). (Right) The maximum separation of any two voxels in the voxelized track.

3 A new topological signature of the primary trajectory

3.1 Features of the energy deposition in CZT

3.1.1 Specific energy loss of the electron in CZT

When transporting through absorbing materials, the electrons may lose their energy in forms of collisional losses and radiative losses, which are described with formulas in Ref. [14]. According to the relevant material parameters of CZT, the specific energy loss of electrons in CZT is shown in Fig. 4.

The resulting length of the electron's track L (NOT *electron range*) as a function of its initial energy E can be described as

$$L = \int_0^{E_0} \frac{1}{-(dE/dx)} dE \quad \text{Eq. 1}$$

To be mentioned, the specific energy loss and length of track of an electron are statistical and may meet large fluctuations. On average, the length of a 2813.50 keV electron's track can be estimated as approximately 3.7 mm. (As comparison, the *electron range* of a 2813.50 keV electron in CZT is approximately 1.5 mm. [15])

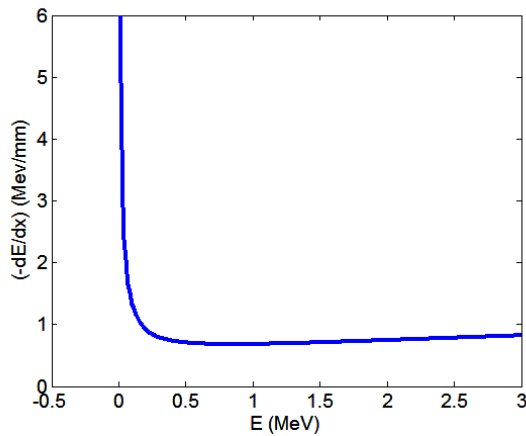


Fig. 4 . Specific energy loss of the electron in CZT

3.1.2 The energy depositions at the endpoints

Fig. 4 shows that specific energy loss of the electron is approximately constant as the energy of the electron decreases along the length of track, until at the end of the track a dramatic increase of the energy loss occurs. This increase causes a significant energy deposition in a compact region, (so-called ‘blobs’), as shown in Fig. 2. Another important reason for the occurrence of blobs in voxelized tracks is that a slower electron at the end of the MC track would meet stronger deflections due to the multiple scattering and thus wrap around in a compact region.

In Fig. 1, the ‘blobs’ can’t be easily found at the endpoints of the MC tracks due to the impact of the large energy fluctuation, which can be reduced after voxelization. As a result, in Fig. 2, the signature of the ‘blobs’ are much clearer: One larger energy deposition at one of the endpoints of the voxelized track can be found in the single-electron event. In contrast, the voxelized track of the $0\nu\beta\beta$ event is characterized by two larger energy depositions at both endpoints of the voxelized track.

3.2 Reconstruction of the primary trajectory

In Fig. 1, the MC tracks of the single-electron events and $0\nu\beta\beta$ events are obtained. It is easy to record the sequence of the points in a MC track according to the time of the energy deposition. However, when it comes to a real detector, it is almost impossible to know the sequence of the energy deposition, because the time difference between the energy depositions is far smaller than the time resolution of the detector. So in a real experiment, what we can measured were only a couple of unorganized points with non-zero energy depositions. In order to reconstruct the real track, the first work is to group the unorganized *points* into a *graph*.

In the *graph theory* in the mathematical field of topology, the *points* are mathematical abstractions for the interconnected objects, and the *lines* describe the connectivity between the *points*. In this article, *points* are defined as the voxelized points (in Fig. 2), and two *points* are connected only when they are close enough. So we define a *connectivity criteria* T , and when the space distance between two *points* is no more than T , the *points* are thought to be connected with a *line*, and the *weight* of the *line* is defined as the space distance.

As the *point’s* space coordinate is voxelized as a whole-number multiple of D , so the space distance between *points* can only be $\sqrt{N} \cdot D$ (N as positive integers, D as the side length of the voxel). In this article, the *connectivity criteria* T is opted to defaulted $\sqrt{3}D$. That is, only if the space distance between two *points* is no more than $\sqrt{3}D$, these two *points* are thought to be connected. An instance of the graph with a *connectivity criteria* $T = \sqrt{3}D$ is shown in Fig. 5.

According to the typical *shortest path problems* in graph theory [16], we calculate the shortest-path between every two *points*, and pick up the longest of such paths, which is defined as the *main path*. If more than one longest path are found, the one with the minimum deflection is selected. An instance of the *main path* (magenta line) is shown in Fig. 5, which can serve as a rough approximation of the MC track. However, the *main path* is drawn from the mathematic calculation, and may sometimes fail to reflect the average position of the electrons.

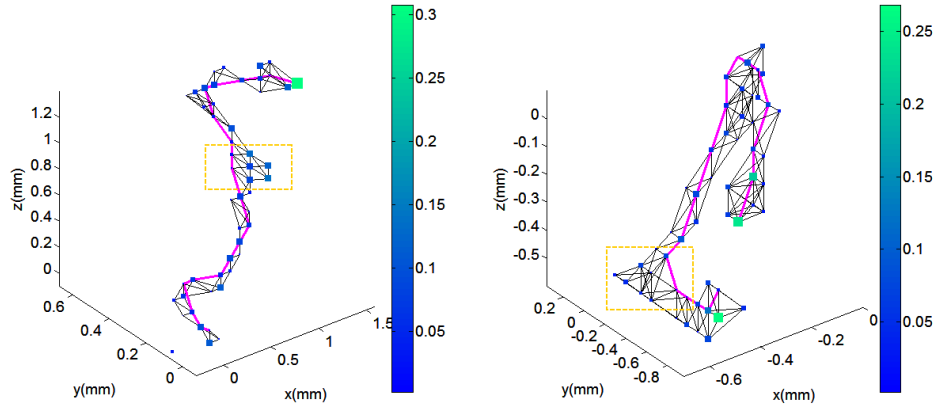


Fig. 5. An instance of the graph ($T = \sqrt{3}D$) of a single-electron event (left) and a $0\nu\beta\beta$ event (right). The reconstructed main path is marked with the magenta line, which fails to mimic the average position of the voxelized track in the orange rectangle.

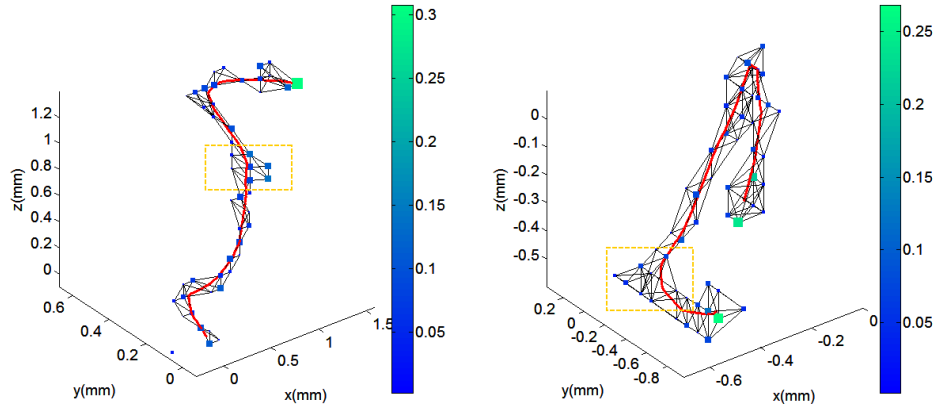


Fig. 6. An instance of the reconstructed primary trajectory of a single-electron event (left) and a $0\nu\beta\beta$ event (right). The primary trajectory is smoother than the main path, and performs better in the orange rectangle.

As an improvement of the *main path*, a spatial filter is established for the smoothing of this polygonal line: Every *point* P_k on the *main path* is replaced by the center-of-gravity J_k of the energy deposition in an R -radius ball around P_k . All the J_k constitute a new line defined as a *primary trajectory* (the red line in Fig. 6). The radius R of the ball initially equals $\sqrt{3}D$, and the influence of the value of R is discussed in section 5.2. The results in section 5.2 will indicate that the *primary trajectory* is a significant improvement compared with the *main path*.

Fig. 7 shows the comparison between the *primary trajectory* and the MC track, which proves that the *primary trajectory* is quite a good approximation of the MC track of the electron, and can be qualified as a crucial topological signature to study the features of electrons.

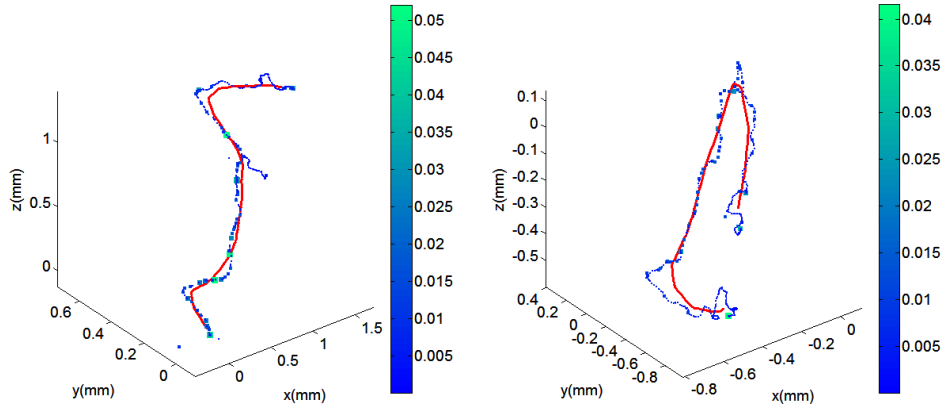


Fig. 7. An instance of the comparison between the MC track and the primary trajectory of a single-electron event (left) and a $0\nu\beta\beta$ event (right). The differences are mainly caused by the information loss during voxelization.

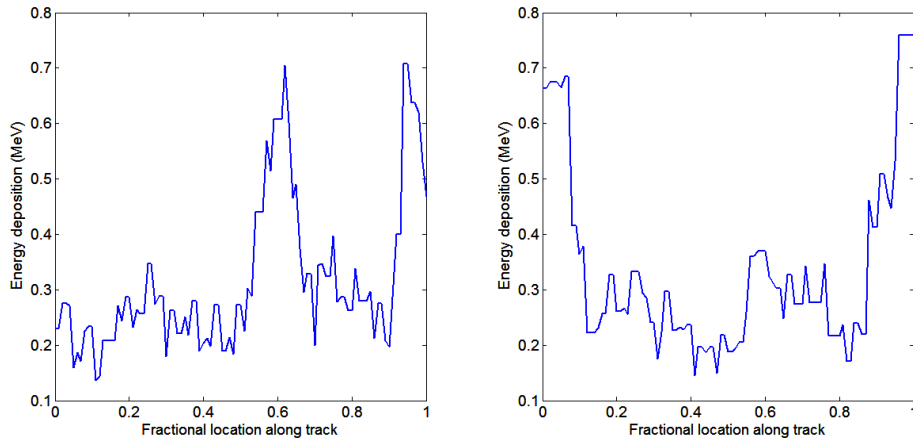


Fig. 8. An instance of the energy deposition along the primary trajectory of a single-electron track event (left) and a $0\nu\beta\beta$ event (right). The topological signature of ‘blobs’ can be found as an energy-deposition peak near the ends of the curve.

3.3 Primary energy deposition along the primary trajectory

With the *primary trajectory* of single-electron and $0\nu\beta\beta$ events, we can calculate the energy deposition in an R -radius ball along the *primary trajectory*, so-called *primary energy deposition*. At every point J_k on the *primary trajectory*, the energy deposition E_k is defined as the sum of the energy in the R -radius ball around J_k .

As the *primary trajectory* of the same type of events may also vary in the length, so J_k is choose at the 0%, 1%... 100% fractional length of the *primary trajectory* (J_0 at 0% and J_{100} at 100% are the two endpoints). As the *primary trajectory* has no direction, so 0% is personally defined as the lower-energy-deposition endpoint of the *primary trajectory* and 100% as the other endpoint (i.e. $E_0 < E_{100}$). For every event, the *primary energy deposition* $E_0, E_1, E_2 \dots E_{100}$ can be calculated.

An instance of the *primary energy deposition* is shown in Fig. 8. The topological signature of ‘blobs’ can be found as an energy-deposition peak near the two ends of the curve.

4 Discrimination methods and results

4.1 Primary energy deposition model

With the simulation method described in section 2, 10^5 samples of single-electron events and 10^5 samples of $0\nu\beta\beta$ events are generated. For each sample, the *primary energy deposition* $E_0, E_1, E_2 \dots E_{100}$ at each fractional length $J_0, J_1, J_2 \dots J_{100}$ are calculated.

For the single-electron samples, the sample mean $\overline{E}_0, \overline{E}_1, \overline{E}_2 \dots \overline{E}_{100}$ and the sample standard deviation $\sigma_0, \sigma_1, \sigma_2 \dots \sigma_{100}$ can be calculated at each J_k . The value of \overline{E}_k reflects the average energy deposition at J_k , and the value of σ_k reflects the fluctuation of the energy deposition at J_k . These features of the single-electron events are shown with red error bar in Fig. 9. Similarly, the features of $0\nu\beta\beta$ events are shown with blue error bar in Fig. 9.

Fig. 9 indicates that the features of the primary energy deposition are apparently different between single-electron events and $0\nu\beta\beta$ events, which establishes a *primary energy deposition model*.

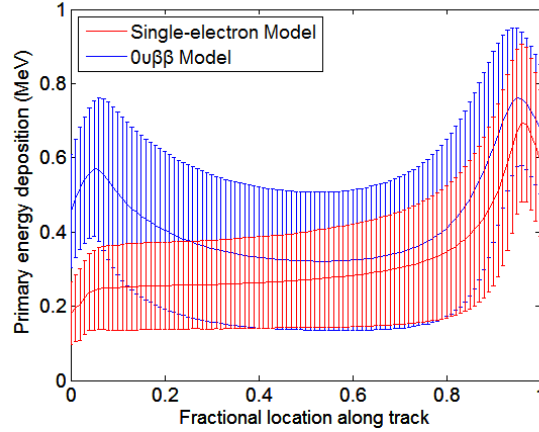


Fig. 9. The primary energy deposition models of the $0\nu\beta\beta$ events and single-electron events. The feature of ‘blobs’ can also be clearly found in the model. There are large deviations of energy deposition in the middle of the trajectory, reflecting the high fluctuation of in energy deposition due to multiple scattering.

4.2 Discrimination methods

The *primary energy deposition models* show the difference between single-electron events and $0\nu\beta\beta$ events, which can be used to identify whether an unknown track is a $0\nu\beta\beta$ event or a single-electron event.

To describe the features of *primary energy deposition*, we define a random vector:

$$\vec{E} = (E_0, E_1, E_2, \dots, E_{100}) \quad \text{Eq. 2}$$

In this view, the discrimination between single-electron events and $0\nu\beta\beta$ events is to find a separation between \vec{E} of single-electron samples and \vec{E} of $0\nu\beta\beta$ samples. One approach to obtain the maximum separation is the Fisher's linear discriminant (see, for instance, Ref. [17]).

A linear combination of features is established:

$$S = \vec{w} \cdot \vec{E} = \sum_{k=0}^{100} w_k \cdot E_k \quad \text{Eq. 3}$$

w_k is the weighting factor for E_k , which indicates the significance of E_k at the fractional distance k . The evaluation of w_k is crucial to the discrimination method. If the samples of \vec{E} in single-electron events have means $\vec{\mu}_S$ and covariance Σ_S , and the samples of \vec{E} of $0\nu\beta\beta$ events have means $\vec{\mu}_D$ and covariance Σ_D , then \vec{w} can be evaluated in Fisher's linear discriminant as:

$$\vec{w} = (\Sigma_D + \Sigma_S)^{-1} (\vec{\mu}_D - \vec{\mu}_S) \quad \text{Eq. 4}$$

The cut c can be evaluated as:

$$c = \vec{w} \cdot \frac{1}{2} (\vec{\mu}_D + \vec{\mu}_S) \quad \text{Eq. 5}$$

If $S > c$, the unknown track is identified as a $0\nu\beta\beta$ event, otherwise $S < c$ as a single-electron event. If in a very special situation with $S = c$, the unknown track is identified as uncertain, but it didn't happen in our data set.

To be mentioned, different value of D (side length of voxel), R (radius of energy-deposition ball), and T (connectivity criteria) will result in different models, thus different w_k and c . However, in general, w_0 is always the largest one of all the w_k , which means the $0\nu\beta\beta$ model and the single-electron model separate from each other most clearly at $k = 0$. It indicates that the energy deposition at the lower-energy-endpoint is always the most significant feature for the discrimination, which is adopted by the NEXT experiment in Ref. [9], for distinguishing single electrons from electron-positron pairs.

4.3 Discrimination efficiency

For every sample represented for a single-electron event or $0\nu\beta\beta$ event, the value of S is calculated and compared with c , thus obtaining the identified result. By comparing the identified results with the real results, we can conclude the discrimination efficiency of both single-electron events and $0\nu\beta\beta$ events.

The discrimination efficiency is influenced by the choice of D , R , and T . In this section, the value is set as $D = 0.1$ mm, $R = \sqrt{3}D$, and $T = \sqrt{3}D$ by default, which means that the side length of the voxel is 0.1 mm, the radius of the energy-deposition ball is $0.1\sqrt{3}$ mm, and the connectivity criteria is $0.1\sqrt{3}$ mm.

The efficiency of the discrimination method is shown in Table I. The single-electron background is rejected with a factor of 93.75%, with an efficiency of 85.44% for $0\nu\beta\beta$ signal events. This efficiency can be regarded as the best consequence which can be obtained in an ideal experiment.

Table I. Efficiency of the discrimination method

Conditions	$D = 0.1$ mm, $R = \sqrt{3}D$, $T = \sqrt{3}D$	
	Single-electron	$0\nu\beta\beta$
Data Set	74062	81005
Efficiency	0.9375	0.8544

5 The effects of the parameters

5.1 The connection criteria T

The *connection criteria T* influences the establishment of the *main path*. Only when the space distance between two *points* is no more than T , the *points* are thought to be connected with a *line*. Different values of T have different implications in the graph:

$T = D$: Two *points* in the graph are thought to be connected if their voxels share a face.

$T = \sqrt{2}D$: Two *points* are connected if their voxels share a face or an edge.

$T = \sqrt{3}D$: Two *points* are connected if their voxels share a face, an edge or a corner.

Among them, the smallest $T = D$ is the most strict criteria, and in this case, the distance between every neighbour points in the *main path* must equals D . As comparison, in a $T = \sqrt{3}D$ criteria, this distance can be D , $\sqrt{2}D$, or $\sqrt{3}D$.

In general, the $T = D$ criteria keeps the most detailed information, as in this case, the *main path* would pass through the greatest number of voxelized points. As a result, the *primary trajectory* reconstructed from the $T=D$ *main path* best mimics the MC track.

However, if the energy resolution of the detector and electronic noise are taking into account, the performance of $T = D$ criteria will degrade. For instance, if the energy deposition of a *point X* in the *main path* falls to zero due to the energy resolution, the *main path* algorithm may probably return two shorter paths instead of the original one, thus resulting in a wrong *main path*.

In this article, for the promising application in real detectors, the *connection criteria T* is set as $\sqrt{3}D$ in order to be more tolerant to the breakpoints due to the noises.

5.2 The radius of the energy-deposition ball R

For one data sample, the value of R influences the effects of the filter, thus resulting in different *primary trajectory*. The filter is effective only when R is larger than D . Otherwise, if $R < D$, only one voxelized point can be found in the energy-deposition ball, so the filter is disabled and the *primary trajectory* and the *main path* are identical. Meanwhile, R should not be too large, since the detailed information of the track will be lost.

This section takes $D = 0.1$ mm, and $T = \sqrt{3}D$ as defaulted condition, and discusses how the variation of R influences the discrimination efficiency. The results are listed in Table II.

TABLE II. Efficiency of the discrimination method with different R

Conditions	$R < D$	$R = D$	$R = \sqrt{2}D$	$R = \sqrt{3}D$	$R = 2D$	$R = \sqrt{5}D$	$R = \sqrt{6}D$	$R = \sqrt{7}D$
Single-electron Efficiency	0.8309	0.9056	0.9312	0.9375	0.9268	0.9214	0.9167	0.9140
$0\nu\beta\beta$ Efficiency	0.7033	0.749	0.8244	0.8544	0.8614	0.868	0.8781	0.8800

Table II shows that the discrimination efficiency of an $R < D$ filter (disabled filter) is much lower than that of an $R = \sqrt{3}D$ filter. Hence, the *primary trajectory* introduced in this article proves a better performance than the *main path* for the discrimination efficiency. And the best filter for a high efficiency for both single-electron events and $0\nu\beta\beta$ events can be found around $R = \sqrt{3}D$.

5.3 The side length of the voxel D

According to the scales of the length of track (about 3.7 mm at 2813.50 keV) described in section 3.1.1, the 3-D spatial resolution of a real detector should be as good as several submillimeters, so as to obtain the topological signatures of an electron's track. In this article, the side length of the voxel is defaulted 0.1 mm ($D = 0.1$ mm) to stand for a spatial resolution of 0.1 mm.

If the spatial resolution of a real CZT detector is larger than 0.1 mm, the performance of this discrimination method began to degrade, in terms of the discrimination efficiency of both single-electron events and $0\nu\beta\beta$ events. We evaluate this degradation by setting a larger value of D , corresponding to the ideal spatial resolution of one detector.

The result of the discrimination efficiency affected by D is shown in Table III. As D alters its value, the value of R should be reappraised. Only the optimal R is listed in the table.

TABLE III. Efficiency of the discrimination method with different D

Conditions	$D = 0.1$ mm $R = \sqrt{3}D.$	$D = 0.2$ mm $R = \sqrt{2}D.$	$D = 0.3$ mm $R = \sqrt{2}D.$	$D = 0.4$ mm $R = D.$	$D = 0.5$ mm $R = D.$
Single-electron Efficiency	0.9375	0.8592	0.8476	0.8345	0.8151
$0\nu\beta\beta$ Efficiency	0.8544	0.8137	0.7952	0.7172	0.7067

As D increases, the loss of the track's information is much more serious, so R/D in the optimal performance should be smaller to reduce further information loss. And $R = D$ provides the smallest R with an effective filter.

Even if the spatial resolution of the CZT detector degrades to 0.5 mm, this discrimination method can still provide an ideal efficiency of 82% for single-electron events and 71% for $0\nu\beta\beta$ events.

5.4 Energy resolution and electronics noise

The data sources in this article are obtained from the GEANT4 simulation, and the conditions of a real experiment are not considered, such as the energy resolution of the detector, the noise of the electronics, and other effects. As a result, the discrimination efficiency discussed in section 4.1 is equivalent to the best consequence obtained in an ideal experiment.

6 Conclusion

A new topological signature '*primary trajectory*' of single-electron events and $0\nu\beta\beta$ events is introduced in this article, as a significant supplement of the topological signature '*main path*'. We discussed the energy deposition along the *primary trajectory* and established the *primary energy deposition model*.

With the distinctions between the models of both event types, this article proposes a new discrimination method called *primary energy deposition discrimination method*. With a criteria of $D = 0.1$ mm, $R = \sqrt{3}D$, and $T = \sqrt{3}D$, a performance with a signal efficiency of 85.44% and a background rejection of 93.75% is concluded. Compared with the lower energy blob method in Ref. [9], this discrimination method may feature in both the robustness and the discrimination efficiency. Though this discrimination method is designed for distinguish single-electron events and $0\nu\beta\beta$

events, it is also proved to be powerful to reject alpha and muons, which makes this method feasible in the real research.

This article also discussed how the value of D , R , and T affects the discrimination efficiency, and evaluated the requirement for the spatial resolution of a real CZT detector. To be mentioned, the results in this article is drawn from the tracks of single-electron and $0\nu\beta\beta$ events generated in the GEANT4 simulation, the influence of energy resolution and electronic noise should be further discussed.

Acknowledgements

This work was supported by the National Natural Science Foundation of China (No. 11305093 & No.11175099) and the Tsinghua University Initiative Scientific Research Program (No. 2011Z07131 & No. 2014Z21016)

References:

- [1]. Gómez-Cadenas, J.J. and J. Martín-Albo, Phenomenology of neutrinoless double beta decay. 2015.
- [2]. Benato, G., Search of Neutrinoless Double Beta Decay with the GERDA Experiment, in proceeding for CIPANP-2015 conference. 2015, eprint arXiv:1509.07792. p. 9.
- [3]. Albert, J.B., et al., Search for Majorana neutrinos with the first two years of EXO-200 data. *Nature*, 2014. 510(7504): p. 229-234.
- [4]. Collaboration, C., et al., Status of the CUORE and results from the CUORE-0 neutrinoless double beta decay experiments. 2015: p. 7.
- [5]. Zuber, K., COBRA—double beta decay searches using CdTe detectors. *Physics Letters B*, 2001. 519(1-2): p. 1-7.
- [6]. Wonsak, B., Status and Perspectives of the COBRA Experiment. *Physics Procedia*, 2015. 61: p. 295-299.
- [7]. Bloxham, T.R. and M. Freer, Evaluation of pixellated CZT detectors for neutrinoless double beta-decay measurements. *Nuclear Instruments and Methods in Physics Research Section A: Accelerators, Spectrometers, Detectors and Associated Equipment*, 2007. 572(2): p. 722-728.
- [8]. Collaboration, N., et al., The NEXT-100 experiment for neutrinoless double beta decay searches (Conceptual Design Report). 2011.
- [9]. Collaboration, N., et al., First proof of topological signature in the NEXT high pressure xenon gas TPC with electroluminescence amplification. 2015: p. 18.
- [10]. Agostinelli, S., et al., Geant4—a simulation toolkit. *Nuclear Instruments and Methods in Physics Research Section A: Accelerators, Spectrometers, Detectors and Associated Equipment*, 2003. 506(3): p. 250-303.
- [11]. Soti, G., et al., Performance of Geant4 in simulating semiconductor particle detector response in the energy range below 1MeV. *Nuclear Instruments and Methods in Physics Research Section A: Accelerators, Spectrometers, Detectors and Associated Equipment*, 2013. 728: p. 11-22.
- [12]. Tretyak, V.I. and Y.G. Zdesenko, Tables of double beta decay data. *Atomic Data and Nuclear Data Tables*, 1995. 61(1): p. 43-90.
- [13]. Filipenko, M., et al., 3D Particle Track Reconstruction in a Single Layer Cadmium-Telluride Hybrid

Active Pixel Detector. 2014.

[14]. Knoll, G.F., Radiation detection and measurement. 2010: John Wiley & Sons.

[15]. Kiel, H., Determination of the Half Lives of Rare Decays of Cd, Te and Zn Isotopes for the COBRA Experiment. 2005.

[16]. Dijkstra, E.W., A note on two problems in connexion with graphs. *Numerische Mathematik*, 1959. 1(1): p. 269-271.

[17]. Cowan, G., Statistical data analysis. 1998: Oxford University Press.